Inorganic Chemistry
Article
pubs.acs.org/IC

Structural and Physical Properties Diversity of New $CaCu_5$-Type Related Europium Platinum Borides

Leonid Salamakha,[†,‡] Ernst Bauer,*[,†] Gerfried Hilscher,[†] Herwig Michor,[†] Oksana Sologub,[§] Peter Rogl,*[,§] and Gerald Giester[∥]

[†]Institute of Solid State Physics, Vienna University of Technology, A-1040 Wien, Austria
[§]Institute of Physical Chemistry and [∥]Institute of Mineralogy and Crystallography, University of Vienna, A-1090 Wien, Austria
[‡]Department of Physics of Metals, Lviv National University, 79005 Lviv, Ukraine

S *Supporting Information*

ABSTRACT: Three novel europium platinum borides have been synthesized by arc melting of constituent elements and subsequent annealing. They were characterized by X-ray powder and single-crystal diffraction: $EuPt_4B$, $CeCo_4B$ type, *P6/mmm*, $a = 0.56167(2)$ nm, $c = 0.74399(3)$ nm; $Eu_3Pt_7B_2$, $Ca_3Al_7Cu_2$ type as an ordered variant of $PuNi_3$, $R\bar{3}m$, $a = 0.55477(2)$ nm, $c = 2.2896(1)$ nm; and $Eu_5Pt_{18}B_{6-x}$, a new unique structure type, *Fmmm*, $a = 0.55813(3)$ nm, $b = 0.95476(5)$ nm, $c = 3.51578(2)$ nm. These compounds belong to the $CaCu_5$ family of structures, revealing a stacking sequence of $CaCu_5$-type slabs with different structural units: $CaCu_5$ and $CeCo_3B_2$ type in $EuPt_4B$; $CeCo_3B_2$ and Laves $MgCu_2$ type in $Eu_3Pt_7B_2$; and $CaCu_5$-, $CeCo_3B_2$-, and site-exchange $ThCr_2Si_2$-type slabs in $Eu_5Pt_{18}B_{6-x}$. The striking motif in the $Eu_5Pt_{18}B_{6-x}$ structure is the boron-centered Pt tetrahedron $[BPt_4]$, which build chains running along the *a* axis and plays a decisive role in the structure arrangement by linking the terminal fragments of repeating blocks of fused Eu polyhedra. Physical properties of two compounds, $EuPt_4B$ and $Eu_3Pt_7B_2$, were studied. Both compounds were found to order magnetically at 36 and 57 K, respectively. For $EuPt_4B$ a mixed-valence state of the Eu atom was confirmed via magnetic and specific heat measurements. Moreover, the Sommerfeld value of the specific heat of $Eu_3Pt_7B_2$ was found to be extraordinarily large, on the order of 0.2 J/mol K^2.

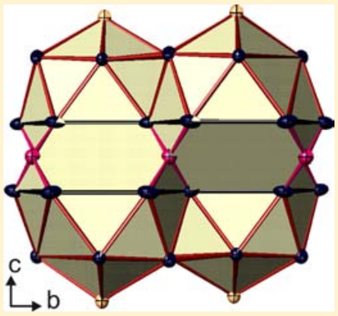

■ INTRODUCTION

Phases with $CaCu_5$-type related structures are frequently found in binary RE−T and ternary RE−T−X (RE = rare-earth metal, T = transition metal, X = B, Si, Al, Ga, Ge, Sn) systems.[1,2] These compounds are extremely diverse in their structural and physical properties. Among them are the following: (i) phases that form by stacking of binary $CaCu_5$-type fragments and slabs of Laves phases with $MgZn_2$ and $MgCu_2$ type (and/or their ternary ordered derivatives)[3] and play an important role for improvement of technological characteristics of RE−Ni-based negative electrode material in Ni−metal hydride batteries;[4] (ii) compounds that can yield magnets appropriate for high-temperature application, namely, $RECo_7$ of $TbCu_7$ type, where part of the atoms in the Ca site of the $CaCu_5$ structure are substituted by the dumbbells of the transition metal and the third element like Ti, Zr, Hf, Cu, Ga, Si, and Ag is required to stabilize the structure and increase the magnetoanisotropy;[5,6] (iii) magnetic materials RE_2Co_{17} revealing the intergrown $CaCu_5$- and Zr_4Al_3-type slabs structures where the interstitial sites can be occupied by elements of IIIA, IVA, or VIA groups, thus leading to the increase in Curie temperature, uniaxial anisotropy, and spontaneous magnetization.[7] The small atomic radius of boron imposes replacement of the Cu atom at the Wyckoff position 2c in the $CaCu_5$ structure (space group *P6/mmm*; Ca in 1a (0,0,0), Cu1 in 2c (1/3,2/3,0), Cu2 in 3g (1/2,0, 1/2)) and formation of the ordered ternary substitution derivative $CeCo_3B_2$ (Ce in 1*a*, Co in 3*g*, and B in 2*c*).[8] As relevant to the study presented herein, the $CeCo_3B_2$ structural unit intergrown with fragments of different structures reveals a variety of borides exhibiting different degrees of structural complexity. For example, the family of structures where the slabs of $CeCo_3B_2$ are stacked with slabs of the binary $CaCu_5$ type or Laves phases are frequently encountered among ternary rare-earth borides with Co and Ni.[1,2,9−12] Formation of these structures in unexplored yet multinary systems may result in unpredicted changes of expected properties, and their investigation is necessary to understand and control the behavior of alloys.

The diversity of $CaCu_5$-derivative structures is enhanced if the ternary rare-earth boride phases with noble metals are considered. For example, (i) the series of compounds formed by stacking blocks of $CeCo_3B_2$ and $CaRh_2B_2$ ($ThCr_2Si_2$) type were observed in Eu−Rh−B,[13] Y−Os−B, and La−Ru−B systems;[14] (ii) $PrRh_{4.8}B_2$ revealed $CeCo_3B_2$-type slabs and hexagon-mesh rhodium nets.[15] In this respect, systems containing Pt and RE metals were not investigated; the only information available on $CaCu_5$-type derivatives concerns the crystal structure and physical properties studies for the $REPt_4B$ series ($CeCo_4B$ type, *P6/mmm*, RE = La, Ce, Pr, Sm).[16,17] In this article we present the results of our exploratory study of the Eu−Pt−B system

Received: July 16, 2012
Published: March 29, 2013

focused on the Pt-rich concentration range where we observed a series of new $CaCu_5$-related structures. Our interest in this investigation was driven not only by the structural flexibility and diversity of $CaCu_5$-type derivative phases but also by the interesting physical properties which europium compounds may exhibit, such as, for example, mixed-valence states or magnetic ordering at comparatively high ordering temperatures, observed in Eu-based binary Laves phases.[18] Results presented herein expand knowledge on a family of $CaCu_5$ derivative structures to (i) the $Eu_5Pt_{18}B_{6-x}$ phase showing a new structural arrangement formed by stacking of inverse $ThCr_2Si_2$-type slabs with $CaCu_5$- and $CeCo_3B_2$-type fragments along the *c*-axis direction, (ii) a new member of rather simple structural series exhibiting the combination of $CaCu_5$- and $CeCo_3B_2$-type slabs, namely, $EuPt_4B$ where a mixed-valence state of Eu has been observed, and (iii) a new compound $Eu_3Pt_7B_2$, composed of $CeCo_3B_2$- and Laves phase- ($MgCu_2$-) type fragments showing interesting transport properties accompanied by a relatively large Sommerfeld coefficient. Structural relationships between the structures are discussed.

EXPERIMENTAL SECTION

Synthesis. All samples, each of a total amount of ca. 0.5−2 g, were prepared by argon arc-melting elemental pieces of europium (99.99%, Metal Rare Earth Ltd., China), platinum foil (99.9%, Ögussa, A), and crystalline boron (98%, Alfa Aesar, D). Due to the low boiling point and high vaporization of europium, Eu weight losses were compensated by adding carefully assigned extra amounts of Eu before melting. For homogeneity, samples were remelted several times. Part of each alloy was wrapped in Mo foil, sealed in an evacuated silica tube, and heat treated for 10 days at 1020 K prior to quench by submerging the capsules in cold water.

X-ray Diffraction Studies. Single crystals suitable for X-ray diffraction studies were isolated from a fragmented annealed alloy of $Eu_3Pt_7B_2$; however, for $EuPt_4B$ and $Eu_5Pt_{18}B_{6-x}$ crystals of good quality were obtained from as cast samples. Crystal quality, unit cell dimensions, and Laue symmetry of the specimens were inspected on an AXS-GADDS texture goniometer prior to X-ray intensity data collections at room temperature on a four-circle Nonius Kappa diffractometer equipped with a CCD area detector employing graphite-monochromated Mo $K\alpha$ radiation (λ = 0.071069 nm). Orientation matrices and unit cell parameters were derived using the program DENZO.[19] No absorption corrections were performed because of the rather regular crystal shapes and small dimensions of the investigated specimens. Space groups were determined from analysis of systematic absences performed with the help of the ABSEN program.[20] Structures were solved and refined with the aid of the WinGX-1.70.00 software package[21] applying SHELXS-97[22] and SHELXL-97[23] programs. Reduced cell calculations and noncrystallographic symmetry tests were performed applying the program PLATON2003[24] in order to check for higher lattice symmetry. Data collection and refinement parameters for the three structures are listed in Tables 1 and 2.

X-ray powder diffraction patterns collected from the $EuPt_4B$ and $Eu_3Pt_7B_2$ alloys annealed at 1020 K for 10 days employing a Guinier−Huber image plate system with monochromatic Cu $K\alpha_1$ radiation ($8° < 2\theta < 100°$) revealed single-phase materials; however, for $Eu_5Pt_{18}B_{6-x}$ several samples synthesized with identical conditions but varying boron concentration were multiphase and contained mixtures with $EuPt_4B$ and/or unknown neighboring phases, suggesting a different temperature range of existence (Figure 1, Supporting Information). Structural parameters obtained from Rietveld powder data refinement[26] of all three compounds validate those from the single crystal.

Physical Properties Studies. Physical properties have been studied for two compounds, $EuPt_4B$ and $Eu_3Pt_7B_2$. The third phase, $Eu_5Pt_{18}B_{6-x}$, is an interesting material with respect to magnetism according to structural and bonding features described below, and currently, special efforts are aimed at optimization of synthesis conditions for this new compound. A superconducting quantum interference device (SQUID) served for determination of the magnetization from 2 to 300 K and in fields up to 7 T where bar-shaped polycrystalline specimens of about 20 mg were used. Specific heat measurements on samples of about 1 g were performed at temperatures ranging from 1.5 to 120 K by means of a quasi-adiabatic step heating technique. Electrical resistivity and magnetoresistivity of bar-shaped samples (about 1 × 1 × 5 mm^3) were measured using a four-probe ac-bridge method in the temperature range from 0.4 K to room temperature and fields up to 12 T.[27]

DETERMINATION AND ANALYSIS OF CRYSTAL STRUCTURES

$Eu_5Pt_{18}B_{6-x}$ (x = 1). Systematic extinctions in the single-crystal X-ray data were consistent with three possible space group types: *Fmmm*, *Fmm*2, and *F*222. The structure was solved in the centrosymmetric space group, and direct methods provided 9 atom positions, 3 of which in further refinement were assigned to europium. Refinement of the structure with all sites fully occupied resulted in rather large anisotropic displacement parameters for two Pt sites (Pt1 in 16*m* and Pt5 in 8*i*) with high residual electron densities (29 000 and 20 000 e/nm^3) near these atoms. Accordingly, the platinum atom sites were split in two near-neighboring positions (Pt1−Pt11 0.037 nm, Pt5−Pt55 0.029 nm) with occupancy parameters refined to 0.8/0.2 for Pt1/Pt11 and Pt5/Pt55. In the next step, all atoms were refined with anisotropic displacement parameters except for the atoms on split sites. Subsequent difference Fourier synthesis revealed two significant residual peaks (about 11 400 and 7000 e/Å^3) at a distance of about 0.2 nm from the nearest platinum atoms, which were attributed to boron atoms (16*m* and 8*f*). Refinement with both boron positions fully occupied led to a low reliability factor (R_F = 0.0353); however, it showed a large isotropic thermal parameter for B2 in 8*f*. Refinement of the B2 occupancy parameter did not improve the value of U_{iso} but reduced the occupancy factor to about 0.5. At this point collected data were also processed in space group *F*222, which provides the possibility to split the B 8*f* site into two crystallographically distinct sites 4*c* (*1/4,1/4,1/4*) and 4*d* (*1/4,1/4,3/4*). Despite almost identical agreement factors, refinement did not improve the isotropic displacement parameters of boron atoms which were found to partially occupy both 4-fold sites (occupancy ratio 33%:67%), suggesting a disordered distribution of boron atoms. The small difference between these solutions concerned also the positions of B1 and the Pt1−Pt11 split sites which all were slightly shifted along the *a* axis due to the free *x* parameter of the 16*k* (*x,y,z*) site (Pt1 x = 0.5010(13), y = 0.1745(2), z = 0.28417(5)/Pt11 x = 0.008(5), y = 0.1455(9), z = 0.2098(2); B1 x = 0.011(12), y = 0.167(2), z = 0.1071(6)). Except these slender deviations, refinement in *F*222 revealed Eu and Pt atoms in the Wyckoff positions corresponding to those in space group *Fmmm*. Accordingly, the test for higher symmetry applying PLATON[24] indicated space group *Fmmm*. Reconsidering the refinement in *Fmmm*, it was found out that the isotropic thermal parameter of B2 can be improved by fixing the occupancy to a predetermined value: in agreement with the results obtained for space group *F*222, the most satisfactory value for the thermal displacement parameter was observed for an occupation factor fixed at 0.5 for B2 in 8*f*. Final refinement in *Fmmm* resulted in a reliability factor as low as 0.0331 and residual electron densities smaller than 3710 e^-/nm^3. Refinement results are given in Table 1.

The structure of $Eu_5Pt_{18}B_{6-x}$, shown in Figure 1a, can be considered as built up of two kinds of blocks alternating along

Table 1. X-ray Single-Crystal Structure Data[a] for $Eu_5Pt_{18}B_{6-x}$

nominal composition	$Eu_{18}Pt_{64}B_{18}$
space group	*Fmmm*; No. 69
structure type	$Eu_5Pt_{18}B_{6-x}$
formula from refinement	$Eu_5Pt_{18}B_{6-x}$ ($x = 1$)
range for data collection	$3.48° < \theta < 29.95°$
cryst size	$35 \times 35 \times 15\ \mu m^3$
a [nm]	0.55813(3)
b [nm]	0.95476(5)
c [nm]	3.51578(2)
Z	4
reflns in refinement	619 $F_o > 4\sigma(F_o)$ of 796
mosaicity	<0.4
no. of variables	52
$R_F^2 = \Sigma\lvert F_0^2 - F_c^2\rvert/\Sigma F_0^2$	0.0331
GOF	1.073
extinction (Zachariasen)	0.000004(3)
M1; occ.; U_{11},[b,c] U_{22}, U_{33}, $U_{23} = U_{13} = 0$, U_{12}	**Eu1** in 8i $(0,0,z)$ $z = 0.29362(5)$; 1.00; 0.0216(9), 0.0137(8), 0.0135(7), 0.0000(0)
M2; occ.; U_{11}, U_{22}, U_{33}, $U_{23} = U_{13} = U_{12} = 0$	**Eu2** in 8i (0,0,z) $z = 0.39475(4)$; 1.00; $U_{11} = U_{22} = 0.0096(7)$, 0.0141(7)
M3; occ.; U_{11}, U_{22}, U_{33}, $U_{23} = U_{13} = U_{12} = 0$	**Eu3** in 4b (0,0,1/2); 1.00; 0.036(2), 0.027(1), 0.017(1)
M4; occ.; U_{11}, U_{22}, U_{33}, U_{23}, U_{13}, U_{12}[d]	**Pt1** in 16m $(0,y,z)$ $y = 0.1742(2)$; $z = 0.21582(5)$; 0.797(4)
	Pt11 in 16m $(0,y,z)$ $y = 0.1437(10)$; $z = 0.2094(3)$; 0.203(4); 0.0305(6), 0.0216(10), 0.0087(8), −0.0023(6), $U_{13} = U_{12} = 0$
M5; occ.; U_{11}, U_{22}, U_{33}, $U_{23} = U_{13} = 0$, U_{12}	**Pt2** in 16j $(1/4, 1/4, z)$ $z = 0.06367(2)$; 1.00; 0.0082(4), 0.0097(4), 0.0120(4), −0.0009(3)
M7; occ.; U_{11}, U_{22}, U_{33}, $U_{23} = U_{13} = 0$, U_{12}	**Pt3** in 16j $(1/4, 1/4, z)$ $z = 0.14811(2)$; 1.00; 0.0079(4), 0.0102(4), 0.0119(4), −0.0006(3)
M9; occ.; U_{11}, U_{22}, U_{33}, $U_{23} = U_{13} = 0$, U_{12}	**Pt4** in 8i $(0, 0, z)$ $z = 0.06519(3)$; 1.000; 0.0092(5), 0.0078(5), 0.0135(5), $U_{12} = 0$
M10; occ.; U_{11}, U_{22}, U_{33}, $U_{23} = U_{13} = 0$, U_{12}[d]	**Pt5** in 8i $(0, 0, z)$ $z = 0.15178(5)$; 0.802(4)
	Pt55 in 8i $(0, 0, z)$ $z = 0.1433(4)$; 0.198(4); 0.0101(6), 0.0081(5), 0.0099(12), $U_{12} = 0$
M11; occ.; U_{11}, U_{22}, U_{33}, $U_{23} = U_{12} = 0$, U_{13}	**Pt6** in 8h $(0, y, 0)$ $y = 0.1622(2)$; 1.00; 0.0322(8), 0.0228(7), 0.0089(5), $U_{13} = 0$
M12; occ.; U_{iso}[b,c]	**B1** in 16m $(0, y, z)$ $y = 0.169(3)$; $z = 0.1070(7)$; 1.00; 0.012(4)
M13; occ.; U_{iso}	**B2** in 8f (1/4, 1/4, 1/4); 0.5; 0.011(12)
residual density; max; min [electrons/nm^3] × 1000	3.71; −3.79

interatomic distances (nm)				
Eu1–2Pt1 0.3128(2)	Eu2–4Pt2 0.3128(1)	Eu3–4Pt6 0.3191(1)	Pt1–2B2 0.1978(1)	Pt11–2B2 0.2239(8)
Eu1–2Pt11 0.3404(1)	Eu2–2Pt4 0.3126(1)	Eu3–2Pt6 0.3225(1)	Pt1–Pt5 0.2797(3)	Pt11–Pt5 0.2443(1)
Eu1–4B2 0.316 (1)	Eu2–4Pt3 0.3149(1)	Eu3–8Pt2 0.3557 (1)	Pt1–Pt55 0. 3044(9)	Pt11–Pt55 0.269(1)
Eu1–2Pt1 0.3201(3)	Eu2–3B1 0.316(3)	Eu3–4Pt4 0.3611(1)	Pt1–Pt1 0.2806(3)	Pt11–Pt11 0.274(1)
Eu1–2Pt11 0.326 (1)	Eu2–3B1 0.322(1)	Eu3–2Eu2 0.3700(1)	Pt1–Pt11 0.315(1)	Pt11–2Pt3 0.2761(9)
Eu1–4Pt1 0.3266(1)	Eu2–2Pt5 0.3234(1)	Pt4–2B1 0.218(3)	Pt1–2Pt3 0.2853(2)	Pt11–Pt1 0.315(1)
Eu1–4Pt11 0.3112(4)	Eu2–2Pt55 0.3095(5)	Pt4–4Pt2 0.2765(1)	Pt1–Eu1 0.3128(2)	Pt11–Eu1 0.326(1)
Eu1–2Pt5 0.3387(1)	Eu2–Eu1 0.3556(2)	Pt4–2Pt6 0.2766(1)	Pt1–Eu1 0.3201(3)	Pt11–Eu1 0.3404(1)
Eu1–2Pt55 0.3565(7)	Eu2–Eu3 0.3700(1)	Pt4–Pt5 0.3044(2)	Pt1–2Eu1 0.3266(1)	Pt11–2Eu1 0.3112(4)
Eu1–4Pt3 0.3441(1)	Pt3–2B1 0.216(2)	Pt4–Pt55 0.2746(11)	Pt5–2B1 0.225(3)	Pt6–2Pt4 0.2766(1)
Eu1–Eu2 0.3556(2)	Pt3–2Pt5 0.27678(2)	Pt4–2Eu2 0.3126(1)	Pt5–4Pt3 0.27678(2)	Pt6–4Pt2 0.2768(1)
Pt2–2B1 0.221(2)	Pt3–2Pt55 0.2770(1)	Pt4–2Eu3 0.3611(1)	Pt5–2Pt1 0.2797(3)	Pt6–Pt6 0.3097(2)
Pt2–2Pt4 0.2765(1)	Pt3–2Pt3 0.2790(1)		Pt5–2Pt11 0.2443(1)	Pt6–2Eu3 0.3191(1)
Pt2–2Pt6 0.2768(1)	Pt3–2Pt1 0.2853(2)		Pt5–Pt4 0.3044(2)	Pt6–Eu3 0.3225(1)
Pt2–2Pt2 0.2791(1)	Pt3–2Pt11 0.2761(9)		Pt5–2Eu2 0.3234(1)	
Pt2–Pt3 0.2968(1)	Pt3–Pt2 0.2968(1)		Pt5–2Eu1 0.3387(1)	
Pt2–2Eu2 0.3128(1)	Pt3–2Eu2 0.3149(1)			
Pt2–2Eu3 0.3557(1)	Pt3–2Eu1 0.3441(1)			
Pt55–2B1 0.206(3)	B1–2Pt3 0.216(2)	B2–4Pt1 0.1978(1)		
Pt55–4Pt3 0.2770(1)	B1–Pt4 0.218(3)	B2–4Pt11 0.2239(8)		
Pt55–2Pt1 0. 3044(9)	B1–2Pt2 0.221(2)	B2–4Eu1 0.3162(1)		
Pt55–2Pt11 0.269(1)	B1–Pt5 0.225(3)			
Pt55–Pt4 0.2746(11)	B1–Pt55 0.206(3)			
Pt55–2Eu2 0.3095(5)	B1–Eu2 0.316(3)			
Pt55–2Eu1 0.3565(7)	B1–2Eu2 0.322(1)			

[a] Crystal structure data are standardized using the program Structure Tidy.[25] [b,c] Isotropic (U_{iso}) and anisotropic atomic displacement parameters (U_{ij}) are given in [10^2 nm^2]. [d] Anisotropic thermal parameters were constrained for the atoms in split positions.

the c direction. One block is composed of two layers of edge-connected triangular prisms which share their faces to form hexagonal channels linked via the 3^6 net of platinum and europium atoms (Figure 1b), while the other one consists of

Table 2. X-ray Single-Crystal Structure Data[a] for EuPt$_4$B and Eu$_3$Pt$_7$B$_2$

parameter/compound	EuPt$_4$B	Eu$_3$Pt$_7$B$_2$
nominal composition	Eu$_{16.7}$Pt$_{66.7}$B$_{16.7}$	Eu$_{25}$Pt$_{58.3}$B$_{16.6}$
space group	*P*6/*mmm*; No. 191	$R\bar{3}m$; No. 166
structure type	CeCo$_4$B	Ca$_3$Al$_7$Cu$_2$
formula from refinement	EuPt$_4$B	Eu$_3$Pt$_7$B$_2$
range for data collection	2.09° < θ < 36.00°	2.16° < θ < 29.98°
cryst size	40 × 40 × 25 μm^3	35 × 35 × 15 μm^3
a [nm]	0.56167(2)	0.55477(2)
c [nm]	0.74399(3)	2.28963(11)
Z	2	3
reflns in refinement	182 $F_o > 4\sigma(F_o)$ of 1069	231 $F_o > 4\sigma(F_o)$ of 777
mosaicity	<0.4	<0.4
no. of variables	14	17
$R_F{}^2 = \Sigma\lvert F_0{}^2 - F_c{}^2\rvert / \Sigma F_0{}^2$	0.0259	0.027
GOF	1.105	1.131
extinction (Zachariasen)	0.0010(3)	0.00050(6)
M1; occ.; U_{11},[b,c] U_{22}, U_{33}, U_{23}, U_{13}, U_{12}	**Eu1** in 1a (0,0,0); 1.00; $U_{11} = U_{22} =$ 0.042(1), 0.035(2), $U_{23} = U_{12} = 0$, 0.0209(6)	**Eu1** in 6c (0,0,z), $z = 0.14405(5)$; 1.00; $U_{11} = U_{22} = 0.0100(4)$, 0.0092(7), $U_{23} = U_{13} = 0$, 0.0050(2)
M2; occ.; U_{11}, U_{22}, U_{33}, U_{23}, U_{13}, U_{12}	**Eu2** in 1b (0, 0, 1/2); 1.00; $U_{11} = U_{22} = 0.0089(6)$, 0.0349(15), $U_{23} = U_{12} = 0$, 0.0044(3)	**Eu2** in 3a (0,0,0); 1.00; $U_{11} = U_{22} = 0.0053(4)$, 0.0074(7), $U_{23} = U_{13} = 0$, 0.0026(2)
M3; occ.; U_{11}, U_{22}, U_{33}, U_{23}, U_{13}, U_{12}	**Pt1** in 2d (1/3, 2/3, 1/2); 1.00; $U_{11} = U_{22} = 0.0494(7)$, 0.0036(5), $U_{23} = U_{12} = 0$, 0.0248(3)	**Pt1** in 18h (x,$-x$,z), $x = 0.49858(3)$, $z = 0.06542(2)$; 1.00; $U_{11} = U_{22} = 0.0044(3)$, 0.0055(1), −0.00005(7), 0.00005(19), 0.0029(3)
M4; occ.; U_{11}, U_{22}, U_{33}, U_{23}, U_{13}, U_{12}	**Pt2** in 6i (1/2, 0, z) $z = 0.19488(8)$; 1.00; 0.0102(3), 0.0070(3), 0.0068(4), $U_{23} = U_{13} = 0$, 0.0035(2)	**Pt2** in 3b (0,0,1/2), 1.00; $U_{11} = U_{22} = 0.0078(4)$, 0.0031(4), $U_{23} = U_{13} = 0$, 0.0039(2)
M5; occ.; U_{11}, U_{22}, U_{33}, U_{23}, U_{13}, U_{12}, U_{iso}[b,c]	**B** in 2c (1/3, 2/3, 0); 1.00; $U_{11} = U_{22} = 0.014(8)$, 0.002(11), $U_{23} = U_{13} =$ 0, 0.007(4)	**B** in 6c (0,0,z), $z = 0.330(1)$; 1.00; $U_{iso} = 0.011(4)$
residual density; max; min [electrons/nm^3] × 1000	4.94; −2.88	4.23; −4.66

interatomic distances (nm)

EuPt$_4$B		Eu$_3$Pt$_7$B$_2$	
Eu1−12Pt2 0.31605(3)	Pt2−2B 0.21751(4)	Eu1−3Pt2 0.32445(2)	Pt1−B 0.216(2)
Eu1−2Eu2 0.37200(2)	Pt2−2Pt1 0.27896(4)	Eu1−3Pt1 0.32636(11)	Pt1−B 0.222(2)
Eu2−6Pt1 0.32428(1)	Pt2−5Pt2 0.2899(1)	Eu1−Eu2 0.32982(12)	Pt1−2Pt1 0.27502(3)
Eu2−12Pt2 0.36113(4)	Pt2−2Eu1 0.31605(3)	Eu1−6Pt1 0.33069(7)	Pt1−2Pt1 0.27975(3)
Eu2−2Eu1 0.37200(2)	Pt2−2Eu2 0.36113(4)	Eu1−3Eu1 0.33662(5)	Pt1−Pt2 0.28098(4)
Pt1−6Pt2 0.27896(4)	B−6Pt2 0.21751(4)	Eu2−12Pt1 0.31525(3)	Pt1−Pt1 0.29959(7)
Pt1−3Eu2 0.32428(1)		Eu2−2Eu1 0.32982(12)	Pt1−2Eu2 0.31525(3)
		Pt2−6Pt1 0.28098(4)	Pt1−Eu1 0.32636(11)
		Pt2−6Eu1 0.32445(2)	Pt1−2Eu1 0.33069(7)
			B−3Pt1 0.216(2)
			B−3Pt1 0.222(2)

[a] Crystal structure data are standardized using the program Structure Tidy.[25] [b,c] Isotropic (U_{iso}) and anisotropic atomic displacement parameters (U_{ij}) are given in [10^2 nm^2].

chains of edge-connected platinum tetrahedra interlinked via europium atoms (Figure 1c). Trigonal prisms are formed by platinum atoms are centered by boron. The 3636 kagomé nets of platinum atoms are slightly puckered, while 3^6 nets are flat. One europium atom, namely, Eu3, is located in the center of a hexagon formed by Pt6 (at $z = 0$), while Eu2 is slightly shifted along z from the B1 atoms plane (Eu2 in 8*i*, $z = 0.39475$; B1 in 16*m*, $z = 0.1070$). Depending on which split position Pt1/Pt11 is locally occupied, the chains of tetrahedra are bridged via (i) europium (for Pt1) or (ii) europium and platinum atoms (for Pt1, Pt11−Pt11 0.2740 nm) to form sheets extending perpendicular to *c*. Platinum tetrahedra are centered by borons; however considering that the B2 site within this block is fractionally (and randomly) occupied (occ. =0.5), one-half of the tetrahedra is empty.

Eu1 is coordinated by 19 atoms revealing the combination of an elongated rhombic dodecahedron with the coordination polyhedron, which is typical for the rare-earth atom in the CaCu$_5$

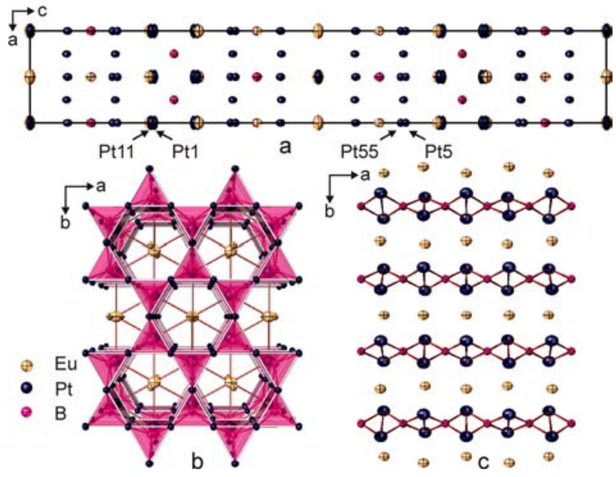

Figure 1. (a) Crystal structure of $Eu_5Pt_{18}B_{6-x}$ with anisotropic displacement parameters for atoms from single-crystal refinement. Atoms in split sites are indicated. (b) Boron-centered Pt triangular prisms (Pt2, Pt3, Pt4, Pt5/Pt55) and 3^6 net of Pt6 accommodating Eu3 atoms at z within 0.33–0.66 (perspective view along the c axis). Eu–Pt bonds within the block of trigonal prisms are omitted. (c) Perspective view of boron-centered Pt tetrahedra (B2 in 8f (1/4, 1/4, 1/4)) along the c axis. Eu1–Pt1 and Eu1–B2 bonds and atoms in split position are omitted.

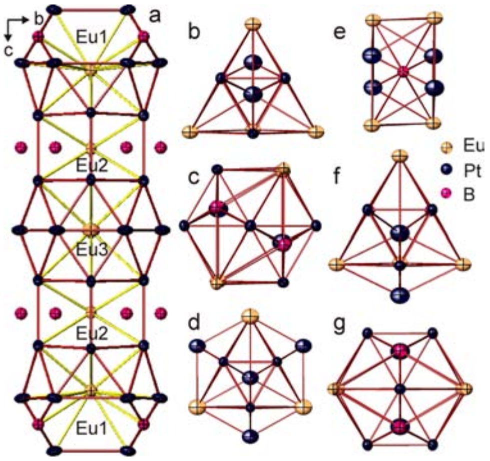

Figure 2. (a) Repeating block of Eu-centered polyhedra in $Eu_5Pt_{18}B_{6-x}$. Eu2–B1 bonds are omitted. (b) Coordination polyhedron of Pt1. (c) Coordination polyhedron of Pt3 as representative of the atom environment for Pt2, Pt4, and Pt5. (d–g) Coordination polyhedra of Pt6 (d), B2 (e), Pt11 (f), and Pt55 (g).

structure. Both fragments are stacked via the hexagon formed by Pt1 atoms (Figure 2a, Table 1). The hexagonal face formed by platinum atoms (Pt3 and Pt5) is capped by a Eu2 atom. The shapes of coordination polyhedra of Eu2 and Eu3 are similar: both atoms are coordinated by 12 Pt atoms forming two hexagonal faces of the coordination sphere. While in the Eu2 polyhedron they are linked by Pt2–Pt3 and Pt4–Pt5 contacts and form a hexagonal prism with the hexagonal faces capped by Eu atoms (Eu1 and Eu3), in the case of Eu3 the distances between the hexagonal faces are long (>0.4 nm) and preclude formation of Pt2–Pt2 and Pt4–Pt4 bonds. The coordination sphere of Eu3 includes also six Pt6 atoms located around the waist of an imaginary hexagonal prism; thus, those 18 platinum atoms form a cage elongated in the direction of the c axis (pseudo-Frank–Kasper polyhedron, which can also be described as two face-connected hexagonal antiprisms) with the hexagonal faces capped by Eu2 atoms. In the case of Eu2, 6 boron atoms centering the rectangular faces of the hexagonal prism are located too far from the central atom to infer strong bonding (Eu2–B2 distances are 0.316 and 0.322 nm).

Pt1 has 10 atoms at coordination distances, and its polyhedron is derived from a tetragonal antiprism (Figure 2b). Pt2, Pt3, Pt4, and Pt5 (Figure 2c) are surrounded by distorted icosahedra with one additional platinum atom; for all four atoms the icosahedra are formed by three almost interperpendicular rectangles made of (i) 4 Pt, (ii) 2 Pt and 2 B, and (iii) 4 europium atoms. The coordination sphere of Pt6 resembles the coordination polyhedron of Cu (2c (1/3, 2/3, 0)) in $CaCu_5$ and includes only platinum and europium atoms (in total 13, 2 of them are at a rather long distance Pt6–2Pt6, 0.3256 nm) (Figure 2d). B1 is coordinated by 6 Pt atoms forming a trigonal prism; three Eu atoms are located against the triangular faces of the trigonal prism (B1–Eu2 0.316 nm and B1–2Eu2 0.322 nm) (Figures 1b and 2a). B2 centers the tetrahedron made of near-neighboring platinum atoms; four Eu atoms complete the coordination sphere, forming a tetragonal antiprism (Figure 2e). The short distances between split positions (Pt1–Pt11 0.03682 nm and Pt5–Pt55 0.03021 nm) and their occupancies (0.80/0.20 for both Pt1/Pt11 and Pt5/Pt55) allow us to assume that on average the Pt1 and Pt5 atoms are present in four of five unit cells while one is filled with Pt11 and Pt55. Coordination spheres for the atoms when the split sites Pt11 and Pt55 are considered replicate the shape of those with (or for) Pt1 and Pt5 differentiating slightly in coordinating distances due to small shifts of atom positions, with the exception of Pt11 which has one more Pt11 in contact distance (Figure 2f and 2g).

$EuPt_4B$. Unit cell dimensions of the $EuPt_4B$ single crystal and X-ray powder diffraction spectra recorded from both the annealed and the as-cast alloys suggested isotypism with $CeCo_4B$-type structure.[1,2,9] Accordingly, the positions of Eu and Pt atoms obtained from structure solution in the space group $P6/mmm$ from the X-ray single-crystal data were consistent with the $CeCo_4B$ type. The atom position of boron was derived from difference Fourier synthesis. Refinement of the structure with anisotropic displacement parameters converged to $R = 0.0259$ with residual electron densities smaller than 4940 e^-/nm^3 and revealed full occupancy of all atom sites (Table 2). The structure of $EuPt_4B$ consists of $CeCo_3B_2$- and $CaCu_5$-type slabs alternating along the c axis. In the coordination sphere of boron ($CeCo_3B_2$-type fragment), six Pt2 atoms are located at equal distance from the central atom, forming a regular triangular prism $[BPt2_6]$ (Figure 3a). Three europium atoms are located against the rectangular faces of the trigonal prism, revealing a B–Eu1 distance 0.32428(1) nm which is larger that the sum of atomic radii of the elements. The trigonal prisms share edges to form hexagonal channels accommodating the Eu1 atoms. Thus, Eu1 is surrounded by 12 Pt2 arranged in the shape of a hexagonal prism; two Eu2 atoms cap the hexagonal prisms of Eu1 at a distance of 0.3720 nm from the central atom (Figure 3b). Similar to the prototype structure and to $Eu_5Pt_{18}B_{6-x}$, Eu2 is located inside a rather large cage elongated along z ($d_{Eu2-Pt2} = 0.3611$ nm) and built of 18 platinum atoms, forming two face-connected hexagonal antiprisms; two Eu1 atoms cap the hexagonal faces. Both atoms in the $CaCu_5$ block (Eu2 and Pt1) reveal unusual thermal displacements: Eu2 exhibits a rather large thermal motion along the hexagonal axis with

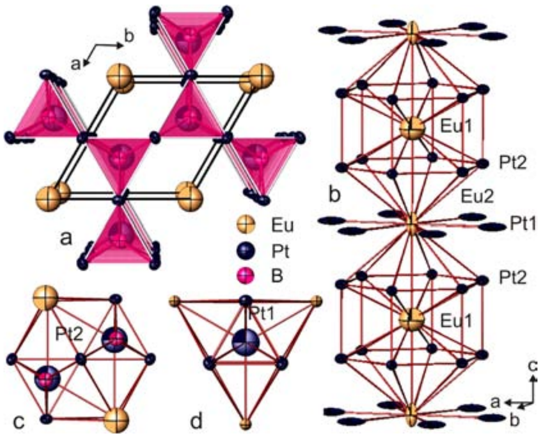

Figure 3. (a) Perspective view of the EuPt$_4$B structure along the *c*-axis direction emphasizing the boron-centered Pt2 triangular prisms. Eu−Pt bonds are omitted. (b−d) Coordination spheres of Eu1 and Eu2 (b), Pt2 (c), and Pt1 (d). Atoms are represented by their thermal ellipsoids. For better visualization, the Pt1−Pt2 bonds are omitted in b.

U_{33}:U_{11}(U_{22}) of ca. 4:1, while Pt1 shows enlarged values U_{11} and U_{22} (U_{11}(U_{22}):U_{33} of about 13). This behavior is illustrated by the thermal ellipsoids in Figure 3b. No fractional or partial occupancies for atom positions were observed from single-crystal data, and refinement of atoms on split positions was not successful. Trial refinements in the space group types with lower symmetry ($P\bar{6}2m$, $P\bar{6}m2$, $P6mm$, $P622$, $P6/m$, $P\bar{6}$, $P6$) yielded inferior results. Comparable features of thermal ellipsoids of atoms located in the channels formed by transition-metal atoms were hitherto also observed for the boride structures related to the CeCo$_3$B$_2$ type, such as In$_5$Ir$_9$B$_4$[28] ($P\bar{6}2m$, a = 0.5590 nm, c = 1.0326 nm) and LaNi$_3$B[29] ($Imma$, a = 0.4970 nm, b = 0.7134 nm, c = 0.8300 nm); for the latter structure, the pronounced anisotropy of the atom thermal displacements prelude the symmetry change upon hydrogenation. In the case of EuPt$_4$B, a possible reason may be that in order to optimize the distance to its Pt2 neighboring atoms Eu2 is delocalized between the layers of Pt2, consequently affecting (since Pt1 and Eu2 are at the same height) the thermal displacements of Pt1. Enlarged displacement parameters of Eu1 are probably indicative of a weak rattling of the europium atom within the 14-atom cage.

Eu$_3$Pt$_7$B$_2$. For Eu$_3$Pt$_7$B$_2$, systematic extinctions characteristic for the trigonal space group $R\bar{3}m$ and unit cell dimensions proposed isotypism with the Ca$_3$Al$_7$Cu$_2$-type structure.[11] Structure solution by direct methods confirmed the arrangement of the heavy atoms analogous to that observed for Ca$_3$Ni$_7$B$_2$[10] (Table 2). The boron position was successfully detected from difference Fourier synthesis. The structure is composed of CeCo$_3$B$_2$- and MgCu$_2$-type fragments alternating along z. Each successive block is shifted with respect to the former one in the (110) plane by a half unit cell. The perspective view of the Eu$_3$Pt$_7$B$_2$ unit cell along the c axis is presented in Figure 4a, showing triangular prisms formed by 6 Pt1 around B. The CeCo$_3$B$_2$-type slabs are formed by 12 Pt1 and 2 Eu1 atoms surrounding Eu2 (Eu2−Pt1 0.31525 nm, Eu2−Eu1 0.32982 nm) to form the bicapped hexagonal prism (Figure 4c). Six boron atoms are located in front of the rectangular faces of the hexagonal prism at the distance 0.3203 nm, which is too long to assume bonding interaction (compare, for example, with Ca$_3$Ni$_7$B$_2$, where $d_{\mathrm{Ca-B}}$ = 0.2978 nm). The coordination polyhedron of Pt2 exhibits a shape analogous to those of transition atoms in the binary MgCu$_2$-type Laves phase: an icosahedron formed by 6Pt1 and 6Eu1 reveals interatomic distances (Table 2) which are comparable with distances in EuPt$_2$[30] (MgCu$_2$ type, Pt−6Pt 0.2727 nm, Pt−6Eu 0.3198 nm). The 16-vertices Frank−Kasper polyhedron [Pt12Eu4] of Eu1 is slightly distorted in comparison with that of Eu in EuPt$_2$ (Figure 4b).

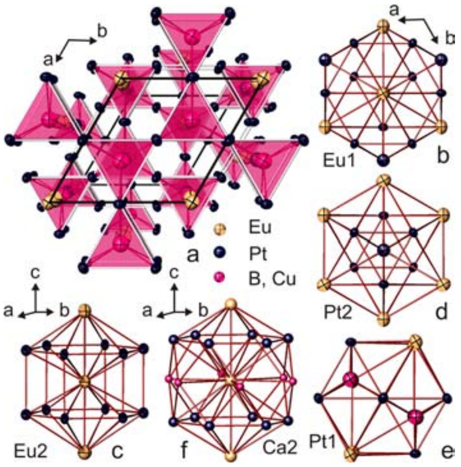

Figure 4. (a) Perspective view of the Eu$_3$Pt$_7$B$_2$ structure along the *c*-axis direction emphasizing the boron-centered Pt1 triangular prisms. (b−e) Coordination spheres of Eu1 (b), Eu2 (c), Pt2 (d), and Pt1 (e). Atoms are represented by their thermal ellipsoids. (f) Twenty-membered cage capturing Ca2 in the Ca$_3$Al$_7$Cu$_2$ structure.

As compared to the prototype Ca$_3$Al$_7$Cu$_2$ structure,[11] significant changes in the coordination sphere of atoms are observed for the CeCo$_3$B$_2$-type block: (i) the distance between the 3636 kagomé net formed by Al atoms is long (about 0.400 nm) in contrast to the corresponding distance between platinum atoms in Eu$_3$Pt$_7$B$_2$ ($d_{\mathrm{Pt1-Pt1}}$ = 0.29959 nm), thus delivering a different shape of the coordination polyhedron of Ca; (ii) due to the larger atomic radius of copper with respect to B, the distance Ca−Cu of 0.324 nm is sufficient to indicate bonding interaction, thus increasing the coordination number of Ca to CN = 20 (Figure 4f) as compared to CN Eu2 = 14 in Eu$_3$Pt$_7$B$_2$. In contrast to EuPt$_4$B, in the present structure none of the atoms show significant anisotropy in their thermal vibration (Table 2).

■ STRUCTURAL RELATIONSHIPS

The investigated structures represent three families of structures revealing the CaCu$_5$-type[31] block in conjunction with other structural fragments. In the discussion below, the structures are arranged in order according to increasing complexity of structural arrangements.

The EuPt$_4$B structure (CeCo$_4$B type[1,2,9]) (Figure 5f) consists of alternating slabs of CaCu$_5$ type (A) (Figure 5a) and slabs of its ternary derivative CeCo$_3$B$_2$ type (B) (Figure 5b). It is a simplest representative of the structural series described in TYPIX[25] under the general formula R$_{m+n}$T$_{5m+3n}$M$_{2n}$, with m = 1, n = 1 (m and n correspond to number of CaCu$_5$-type and CeCo$_3$B$_2$-type blocks, respectively). Similar to the prototype structure, the hexagonal channels filled with Eu are formed by edge-connected trigonal prisms [BPt$_6$] in EuPt$_4$B and alternate with 18-membered platinum cages, capturing europium atoms along the c axis. While in the CeCo$_4$B structure the B atoms are located at 0.2889 nm from the central Ce atom and assume bonding, this distance is rather long in the europium isotype with platinum.

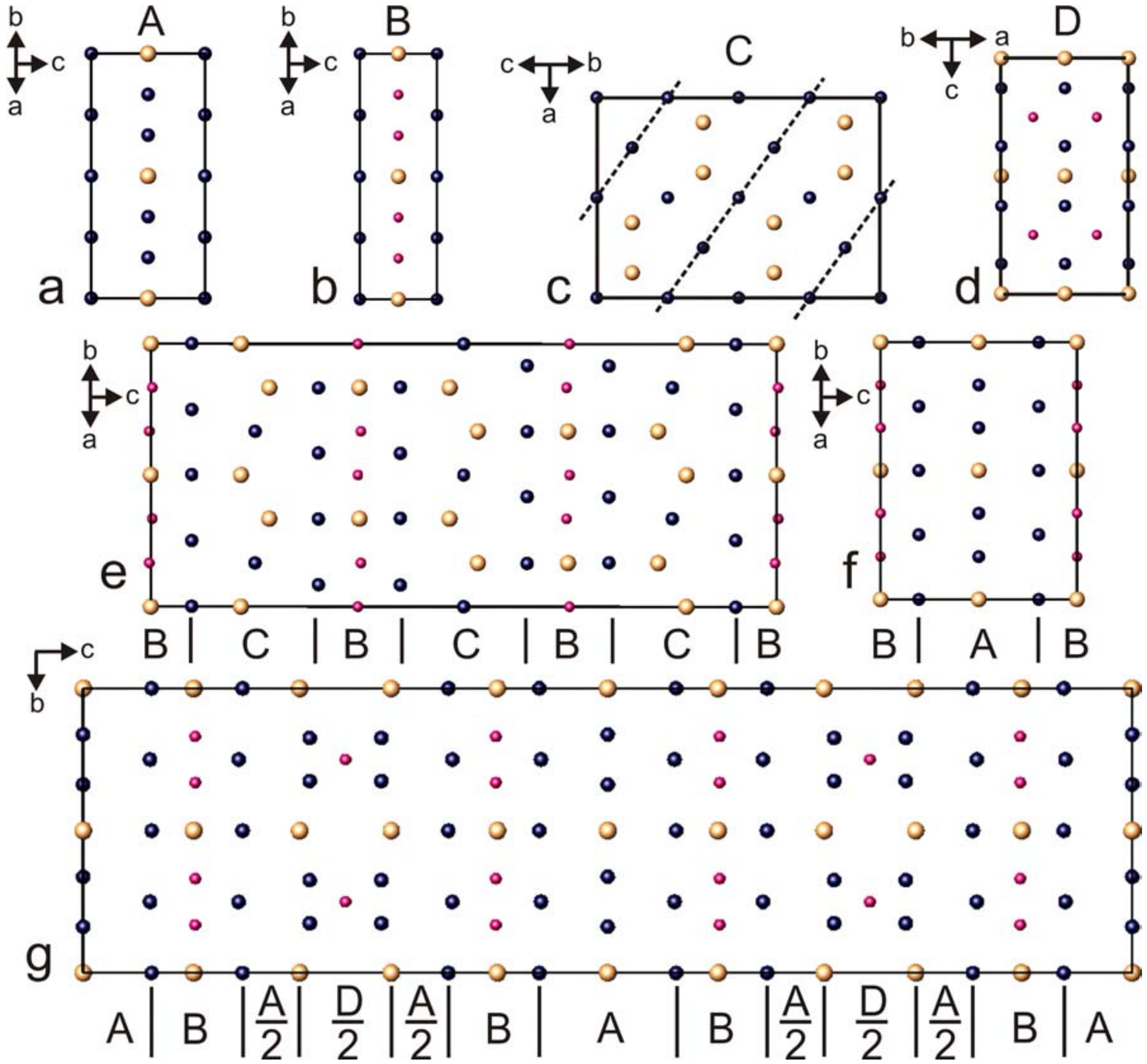

Figure 5. (a) $CaCu_5$- and (b) $CeCo_3B_2$-type structures (for both structures the origin is shifted by 0,0,1/2). (c) $EuPt_2$ structure ($MgCu_2$ type, space group $Fd\bar{3}m$, origin shift 1/4, 0, 3/4). Slabs of $Eu_3Pt_7B_2$ are outlined. (d) Inverse $ThCr_2Si_2$-type structure.[36] (e–g) Structural relationships for (e) $Eu_3Pt_7B_2$, (f) $EuPt_4B$, and (g) $Eu_5Pt_{18}B_{6-x}$ structures. Relative arrangements of structural blocks are indicated with symbols A, B, C, and D.

In contrast to the relatively small unit cell and simple structure of $EuPt_4B$, the two remaining structures, $Eu_3Pt_7B_2$ and $Eu_5Pt_{18}B_{6-x}$, exhibit rather large unit cells and nontrivial stoichiometries.

$Eu_3Pt_7B_2$ is an ordered variant of the $PuNi_3$ type.[32] This binary compound belongs to the rhombohedral branch of a structural series formed within composition range RM_2–RM_5 by stacking the fragments of $CaCu_5$ type and Laves phase and can be described by the formula $R_{2m+n}M_{4m+5n}$, where m accounts for the number of Laves-type slabs (R_2M_4) and n is a number of $CaCu_5$-type slabs.[1−3] Since only the structures with $m = 1$ have been observed for binary structures, the ternary representatives of this series which are built by combining $CeCo_3B_2$- and Laves-type structural slabs ($Ca_3Ni_7B_2$,[10] $Ce_2Ir_5B_2$[12]) follow the formula $R_{2+n}M_{4+3n}X_{2n}$: $2MgCu_2 + nCeCo_3B_2$. The ordered version of $PuNi_3$ was first identified in the Ca–Al–Cu system.[9] In $Ca_3Al_7Cu_2$-type structures with boron ($Ca_3Ni_7B_2$, $Eu_3Pt_7B_2$), the transition-metal atoms adopt the sites of aluminum in the $MgCu_2$-type block and boron atoms replace copper in the $CaCu_5$-type block. Figure 5e shows the arrangement of $CeCo_3B_2$-type slabs (B) and $MgCu_2$-type slabs (C) in the $Eu_3Pt_7B_2$ structure.

The structure of $Eu_5Pt_{18}B_{6-x}$ represents a new type of ternary borides. It can be considered as an intergrowth of three kinds of structure blocks (Figure 5g): one is a $CaCu_5$ type (A), the second having the atom arrangement of its ordered ternary derivative $CeCo_3B_2$ (B), and the third reveals the slab of the site-exchange variant of the $ThCr_2Si_2$ structure with B atoms adopting the sites of Cr (D). The body-centered structure of $ThCr_2Si_2$ (space group $I4/mmm$, Th in $2a$: 0, 0, 0; Cr in $4d$: 0, 1/2, 1/4, Si in $4e$: 0, 0, z), an ordered variant of $BaAl_4$, is widely distributed among RET_2X_2 compounds (T = transition metal, X = p element).[33] The unit cell of $ThCr_2Si_2$ can be described as a stacking of infinite layers of interconnected tetragonal [Cr_4] pyramids around the Si atom (Wyckoff position $4e$, commonly named as pyramidal site) running perpendicular to the c axis with a layer of thorium atoms between these pyramids. Cr atoms are tetrahedrally surrounded by four Si atoms (Wyckoff position $4d$, tetrahedral site). Chemical bonding, atomic site preferences as a function of electronegativity of the constituent elements, size effect with respect to the structural stability, phase widths, and physical properties have been studied for different combinations of the elements[34−41] and particularly developed recently for pnictides due to discovery of superconductivity in the series of iron arsenides with $ThCr_2Si_2$ type.[42−44] Ternary rare-earth borides with a $ThCr_2Si_2$-type structure are quite rare except for few representatives, such as $RECo_2B_2$ (RE = Y, La, Pr, Nd, Sm, Gd−Er),[45−47] $REFe_2B_2$ (RE = Y, Gd−Tm, Lu),[48] and $BaRh_2B_2$.[49] In all these structures the transition metal occupies the atom site of Cr and boron is placed in the position of Si. Accordingly, each T atom is coordinated by four B atoms; a recent reinvestigation of the $ThCr_2Si_2$ type $LaCo_2B_2$ (a = 0.36108 nm, c = 1.02052 nm, z = 0.3324(5)) revealed a relatively short Co−B bond (e.g., 0.20 nm), indicating certain compression of the CoB layer along the c axis and an elongated La−B contact distance (0.308 nm).[50]

There are two $BaAl_4$-type derivative structures encountered for composition RET_2X_2: the structures of $ThCr_2Si_2$ (described above) and $CaBe_2Ge_2$, which is built by intergrowth of $ThCr_2Si_2$-type slabs and slabs of its site-exchange variant along the [001] direction (and thereby one-half of T and X atoms occupy the tetrahedral and pyramidal sites and vice versa, respectively). As reported by Parthe et al.,[36] formation of compounds revealing only inverse $ThCr_2Si_2$-type arrangement is rare; however, this arrangement occurs as slabs in intergrown structures (for example, in $CeNiSi_2$, $BaCuSn_2$, $La_3Co_2Sn_7$). Among borides, formation of inverse $ThCr_2B_2$-type structure was found for $ZnIr_2B_2$ where layers of edge-connected $[BIr_4]$ tetrahedra (Ir in 4e (0, 0, z, z = 0.37347), B in 4d (0, 1/2, 1/4)) are separated by 4^4 networks of zinc atoms (Zn in 2a (0, 0, 0)).[51] Similarly, in $Eu_5Pt_{18}B_{6-x}$, four atoms of platinum form tetrahedra around boron atoms, however exhibiting a higher degree of compression along the b axis: the Pt1−B distance in the $Eu_5Pt_{18}B_{6-x}$ is 0.1978(1) nm (and 0.2239(8) nm for Pt11 in split position) as compared to the length of the Ir−B bond of 0.2150 nm in $ZnIr_2B_2$ showing the tetrahedral angles 2 × 137.07°, 2 × 105.25°, 2 × 90.27° in $Eu_5Pt_{18}B_{6-x}$ (2 × 126.09°, 2 × 100.79°, 2 × 102.91° for Pt11) and 4 × 121.68°, 2 × 87.11° in $ZnIr_2B_2$. Because of limited spatial dimension of the $ThCr_2Si_2$ slab in the $Eu_5Pt_{18}B_{6-x}$ structure (i.e., one-half a unit cell cut along (111)), the tetrahedra do not form infinite layers but are arranged in one-dimensionally linked chains running infinitely along the a axis. Previous theoretical studies based on Mülliken overlap population analysis suggested that the element with greater electronegativity is more strongly bound in the 4e site.[52,53] The atoms site preferences in the structures of three discussed borides (i.e., $LaCo_2B_2$, $ZnIr_2B_2$, and $ThCr_2Si_2$ block in the $Eu_5Pt_{18}B_{6-x}$) are consistent with the electronegativity on the Pauling scale of boron, relative to those of transition elements Co, Ir, and Pt.

Among a large family of reported ternary rare-earth transition-metal borides, the Eu phases are usually missing. For only a few $CaCu_5$-type derivative ternary borides with europium have the precise structural parameters and physical properties been investigated. These are (i) the $Eu_2Rh_5B_4$ and $Eu_3Rh_8B_6$ structures composed of the $CeCo_3B_2$- and $CaRh_2B_2$-type fragments,[54] (ii) $Eu_3Ni_7B_2$ of $CeCo_4B$ type exhibiting one nickel site partially occupied by a mixture of europium and nickel atoms.[55] In both $Eu_2Rh_5B_4$ and $Eu_3Rh_8B_6$ compounds, the Eu atoms have been found in the divalent state, revealing magnetic moments only slightly smaller than the theoretical value of 7.94 μ_B.[54] $EuIr_2B_2$ of $CaRh_2B_2$ type can be considered as a metal-deficient derivative structure of $CeCo_3B_2$; according to a plot of the unit cell volumes vs lanthanide atomic number, Eu was found to be divalent.[56] Comparing the interatomic distances and relating them to the magnetic properties, one can see that in both $Eu_2Rh_5B_4$ and $Eu_3Rh_8B_6$ (Eu $4f^7$) the Eu−Eu distances are 0.3207, 0.3654 nm and 0.3113, 0.3614 nm respectively, while Eu−Rh distances vary between 0.3079 and 0.3256 and 0.3054 and 0.3279 nm. $EuIr_2B_2$ shows similar distance variations: the Eu−Eu bond is 0.3852 nm, and the distances Eu−Ir are 0.3058 and 0.3313 nm. The differences in bond length analogous to $Eu_2Rh_5B_4$, $Eu_3Rh_8B_6$, and $EuIr_2B_2$ can be found in $EuPt_4B$, where one Eu atom, namely, Eu1 ($CeCo_3B_2$-type block) exhibits rather short contacts with Pt2 of 0.31605 nm, whereas Eu2 ($CaCu_5$-type block) exhibits Pt neighbors at 0.32428 and 0.36113 nm. There is one rather long bond between europium atoms Eu1−Eu2 0.3720 nm in $EuPt_4B$. The deviations of the lattice parameters of the europium compound from the lanthanoid contraction in the $REPt_4B$ series also confirm the assumption that Eu is not trivalent in $EuPt_4B$ (Figure 6).

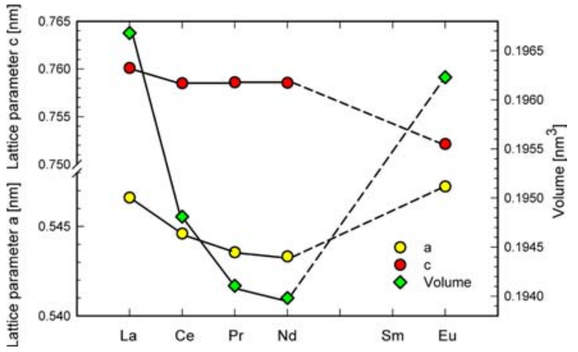

Figure 6. Lattice constants of the $REPt_4B$ series. Values for La−Pr and Nd are taken from the literature.[16] For the europium compound, lattice parameters were obtained from Rietveld refinement of single-phase $EuPt_4B$ alloy used for physical properties measurements.

Similarly, in $Eu_5Pt_{18}B_{6-x}$ the Eu−Eu contacts are long and the distances between Eu and Pt atoms are rather heterogeneous, ranging within 0.3128 and 0.3611 nm.

■ MAGNETIC PROPERTIES

In order to obtain the electronic configuration (EC) of the Eu ions and thus the magnetic state, the magnetization of $EuPt_4B$ and $Eu_3Pt_7B_2$ was measured and analyzed in detail. The temperature dependence of the magnetization and susceptibility for various fields is presented in Figures 7 and 8, respectively.

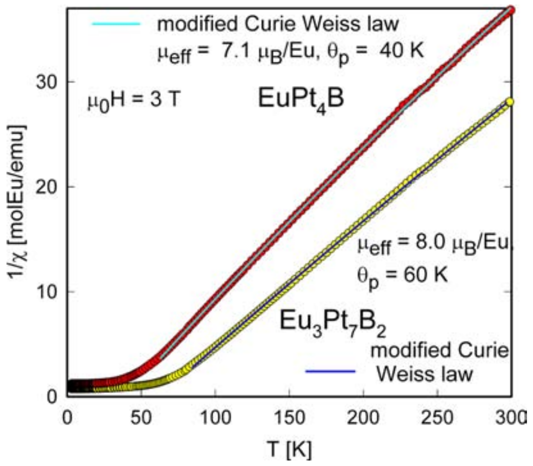

Figure 7. Temperature-dependent inverse magnetic susceptibility of $EuPt_4B$ and $Eu_3Pt_7B_2$. Solid lines are fits according to the modified Curie−Weiss law.

Magnetic susceptibility data $\chi = M/H$ scale pretty well for 0.1, 1, and 3 T above the ordering temperature being indicative that the samples are free from magnetic impurities and other

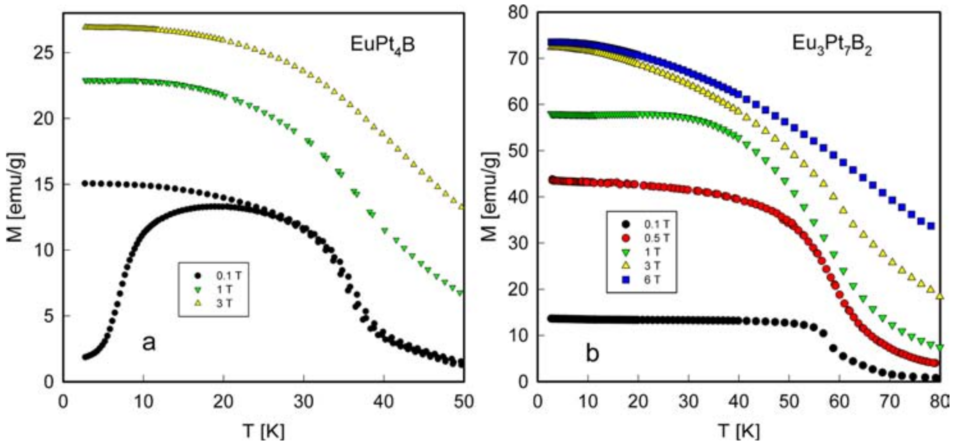

Figure 8. Temperature-dependent magnetization of EuPt$_4$B (a) and Eu$_3$Pt$_7$B$_2$ (b).

magnetic secondary phases; data are displayed in Figure 7 as χ^{-1} vs T for the 3 T run, only.

Both EuPt$_4$B and Eu$_3$Pt$_7$B$_2$ are found to order ferromagnetically. Eu$_3$Pt$_7$B$_2$ shows a transition at 57 K, while EuPt$_4$B orders below 36 K as determined from low-field magnetization measurements and corresponding Arrott plots (see below). The magnetic susceptibility in the paramagnetic region is accounted for by the modified Curie–Weiss law $\chi = \chi_0 + C/(T - \theta_P)$. The paramagnetic Curie temperatures θ_P = 60 and 40 K together with effective magnetic moments μ_{eff} = 8.0 and 7.1 μ_B per Eu atom (derived from the Curie constant, C), were obtained as a result of least-squares fits to the susceptibility data of Eu$_3$Pt$_7$B$_2$ and EuPt$_4$B, respectively (solid lines, Figure 7), with a temperature-independent susceptibility χ_0 of about 3 × 10^{-6} cm^3/g for both compounds. While the paramagnetic moment of Eu$_3$Pt$_7$B$_2$ recounted per one europium atom is almost that expected for the theoretical value of the free Eu^{2+} ion (μ_{eff} = 7.94 μ_B) the effective moment obtained for EuPt$_4$B is significantly smaller, pointing to a mixed- or -intermediate valence state of Eu. The fact that Eu in EuPt$_4$B possesses two inequivalent lattice sites suggests that the more static case (i.e., mixed valence) might account. In such a case, the system can be treated as a mixture of Eu^{2+} and Eu^{3+} atoms located either at the 1(a) or the 1(b) site. Following this approach, the paramagnetic moment of Eu in EuPt$_4$B can be represented as $\mu_{eff} = \sqrt{x{\mu_{Eu^{2+}}}^2 + (1{-}x){\mu_{Eu^{3+}}}^2}$. Here we use a mean literature value for the effective moment of Eu^{3+} with $\mu_{Eu^{3+}}$ = 3.5 μ_B[57,58] rather than the theoretically vanishing effective magnetic moment of a pure Eu^{3+} state. The fraction x of Eu atoms in the 2+ state is thus estimated to be x = 0.75, whereas a vanishing effective moment for the Eu^{3+} state gives a fraction of 80% in the Eu^{2+} state. Although the latter is presumably an overestimate, analysis of the saturation magnetization and heat capacity (see below) supports these assumptions.

The temperature-dependent magnetization, displayed in Figure 8 for various fields, exhibits for EuPt$_4$B significant irreversibilities of the magnetization for zero-field cooling (ZFC) and field cooling (FC) which disappear only for fields larger than 1 T. These irreversibilities can be attributed to domain wall pinning associated with a remarkable hysteresis and a coercivity of 0.32 T at 2.8 K (see Figure 9) as a consequence of the magnetocrystalline anisotropy due to the CaCu$_5$ building blocks. On the contrary, there is hardly any difference for ZFC and field cooling detectable even in the low-field regime for Eu$_3$Pt$_7$B$_2$ yielding also reversible magnetic isotherms without a significant hysteresis, which means the coercivity is 3 orders of magnitude smaller than for EuPt$_4$B.

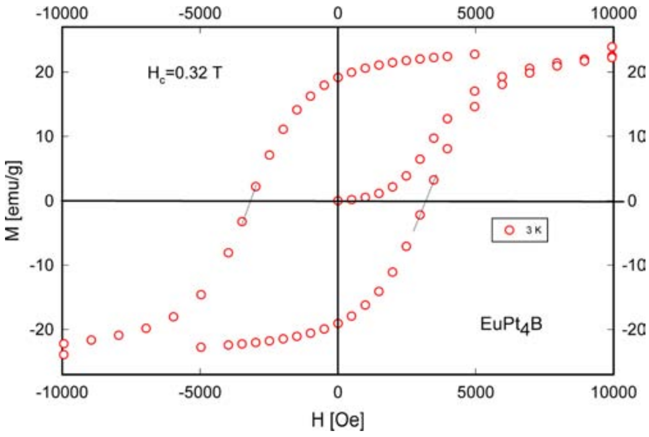

Figure 9. Hysteresis in magnetization of EuPt$_4$B.

A comparison of the magnetic isotherms of both compounds is shown in Figure 10, where the isotherms are displayed as M^2 versus H/M plots (Arrott plots). It should be noted that in the case of EuPt$_4$B with the pronounced hysteresis only the demagnetization data, where the rotation of the magnetization plays the dominant role, are used for the Arrott plots. Deviations from the expected linear behavior of the Arrott plots are observed frequently, see, e.g., ref 59 and references therein, in particular with a curvature symmetrical with respect to T_c, i.e., a negative curvature at $T < T_c$ and a positive curvature at $T > T_c$. This is indeed observed for EuPt$_4$B (Figure 10a), and such symmetrical deviations about T_c can be attributed to spatial variations of the magnetization and/or spin fluctuations. As we have a stoichiometric compound these deviations may arise from fluctuating moments associated with significant thermal motions of Eu2 along the hexagonal axis and/or with the proposed weak rattling of the Eu1 atoms within the 14-atoms cage rather than from a heterogeneous magnetization. On the other hand, it was shown that a substantial uniaxial magnetocrystalline anisotropy causes a remarkable downturn of the Arrott plots below T_c.[60] In this model, the negative curvature of the Arrott plots below T_c can be accounted for as a result of domain rotations in the nonoriented crystallites and against the random but uniaxial anisotropy fields H_A. A rather simple way to estimate H_A in terms of this model is to extrapolate the linear part of the Arrott plot backward

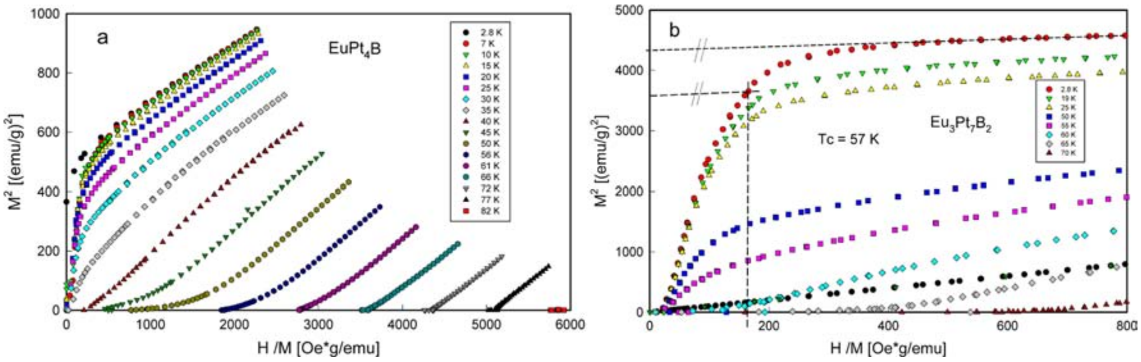

Figure 10. Arrott plots of EuPt$_4$B (a) and Eu$_3$Pt$_7$B$_2$ (b). Dashed lines are used to estimate H_A through the procedure explained below.

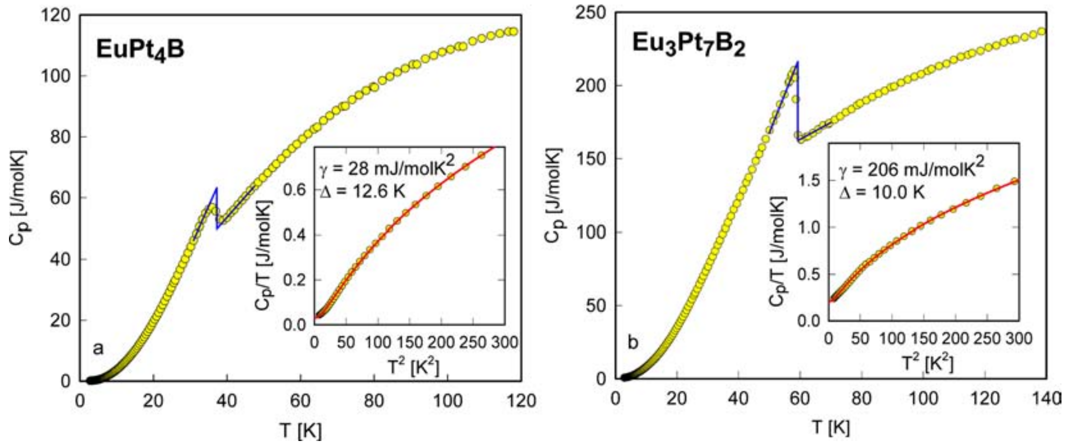

Figure 11. Temperature-dependent specific heat C_p of EuPt$_4$B (a) and Eu$_3$Pt$_7$B$_2$ (b). Solid lines idealize the ferromagnetic phase transition. (Insets) Low-temperature details together with least-squares fits (solid lines) based on a ferromagnetic spin wave model.

to obtain the spontaneous magnetization, and taking 91.3% of that value gives with a parallel forward extrapolation an intersection with the experimental Arrott plot, yielding a value for H/M where this particular field corresponds to the anisotropy field H_A (see the dashed lines in Figure 10b; for further details see ref 59). Using this simple estimate we obtain for Eu$_3$Pt$_7$B$_2$ an anisotropy field of about 1 T which arises from the uniaxial anisotropy of the building blocks.

Although the magnetization at 7 T at 2.8 K is not in a fully saturated state for both compounds we use that value for the saturation magnetization M_S, while the spontaneous magnetization M_0 is obtained from the backward extrapolation of the Arrott plot as mentioned above. This yields for Eu$_3$Pt$_7$B$_2$ M_S = 7.43 μ_B/mol-Eu and M_0 = 7.24 μ_B/mol-Eu and for EuPt$_4$B M_S = 5.13 μ_B/mol-Eu and M_0 = 3.85 μ_B/mol-Eu. Both the saturation as well as the spontaneous magnetization of Eu$_3$Pt$_7$B$_2$ is well above the value expected for a Eu^{2+} ion ($M_s = gj = 7\ \mu_B$), indicative that a substantial 5d conduction electron polarization contributes to the total moment. The significant smaller saturation and spontaneous moment of EuPt$_4$B indicate, in line with results for the effective moments, a mixed-valence state. Under the assumption that the conduction electron polarization is of similar magnitude in both compounds, the ratio of their saturation moments indicates that 69% of the Eu ions are in the Eu^{2+} state in EuPt$_4$B, while a somewhat smaller fraction of about 53% is obtained using the ratio of the spontaneous moments. The latter is an underestimate caused presumably by the large high-field susceptibility of EuPt$_4$B also visible in the larger slope of the Arrott plot in comparison to that of Eu$_3$Pt$_7$B$_2$.

■ SPECIFIC HEAT

Further information on the ground state properties of EuPt$_4$B and Eu$_3$Pt$_7$B$_2$ can be gained from specific heat measurements. Experimental results are shown in Figure 11.

Both EuPt$_4$B and Eu$_3$Pt$_7$B$_2$ exhibit distinct λ-like anomalies around 35 and 57 K, respectively, idealized in Figure 11 by solid lines, which can be attributed to a second-order phase transition of magnetic origin. A nonmagnetic isostructural compound to be used as an analogue was not available for a full comparative analysis. However, it is easily seen that the height of the anomaly δC_p = 56 J/mol·K in the case of Eu$_3$Pt$_7$B$_2$ corresponds well to a mean-field-like transition of a $j = 7/2$ system ($\delta C_p = N{*}5R[j(j+1)/(2j^2+2j+1)]$, where N is the number of RE atoms/mol. Considering three Eu^{2+} atoms per mole yields δC_p = 60.39 J/mol·K, in fair agreement with experiment. The jump of the specific heat of EuPt$_4$B right at the magnetic phase transition temperature is only about 13 J/mol·K in comparison with the expected value of 20.13 J/mol·K. This reveals that only a fraction of the Eu ions is involved in magnetic ordering (i.e., 65% Eu^{2+} and 35% Eu^{3+}), which is in line with the broad range of estimates from the magnetic data where we obtained 53% Eu^{2+} as a lower and 80% Eu^{2+} as an upper limit.

Low-temperature heat capacity data were analyzed in terms of a ferromagnetic spin wave model including a spin wave gap Δ, i.e., $C_p = \gamma T + \beta T^3 + \delta T^{3/2}\exp(-\Delta/T)$ with γ the Sommerfeld value and β proportional to the low-temperature Debye temperature θ_D^{LT} ($\theta_D^{LT} = ((1944N)/\beta)^{1/3}$. Such an analysis should hold for temperatures well below the Curie temperature.

Results of least-squares fits are shown as solid lines in the insets of Figure 11, revealing excellent agreement with γ = 28 and 206 mJ/mol·K^2, resulting in an effective 68 mJ/mol·K^2 per europium atom, β = 0.000222 and 0.000702 J/mol·K^4, δ = 0.36 and 0.46 J/mol·K$^{3/2}$, and Δ = 12.6 and 10 K for $EuPt_4B$ and $Eu_3Pt_7B_2$, respectively. The corresponding Debye temperatures are 370 and 321 K, respectively. Both Eu-based compounds are characterized by Sommerfeld values well beyond simple metals, pointing to strong electron correlations induced by intra-atomic 4f−5d exchange in Eu^{2+} ions in combination with a significant hybridization of Eu and Pt 5d orbitals. The latter is also corroborated by the high saturation magnetization of $Eu_3Pt_7B_2$ which significantly exceeds the expected saturation moment of free Eu^{2+} ions. We note that largely enhanced Sommerfeld values due to f−d exchange have been reported for various Gd intermetallics such as Gd_3Co,[61] Gd_3Rh,[62] and Gd−Ni[63] binaries.

■ ELECTRICAL RESISTIVITY

We studied the electrical resistivity ρ of $EuPt_4B$ and $Eu_3Pt_7B_2$ from 0.3 K to room temperature (see Figure 12). Data evidence metallic behavior in both cases with rather low overall resistivities. Unlike $Eu_3Pt_7B_2$, in the resistivity curve of $EuPt_4B$ a slight change of slope is observed at around 240 K, pointing to some additional, unanticipated scattering processes. For both compounds, anomalies of $\rho(T)$ characterize the magnetic phase transition.

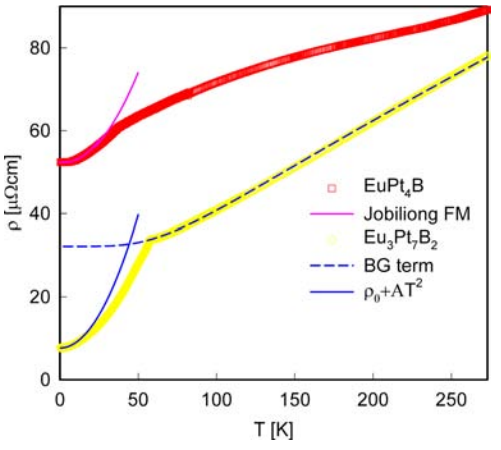

Figure 12. Temperature-dependent electrical resistivity ρ of $EuPt_4B$ and $Eu_3Pt_7B_2$. Lines correspond to models mentioned in the text.[64]

Figure 13 represents the magnetic field dependence of the resistivity of $Eu_3Pt_7B_2$ and $EuPt_4B$. Although the anomaly in both compounds is of ferromagnetic origin, application of a magnetic field causes different responses of the resistivity. The resistivity of $EuPt_4B$ decreases slightly in the entire temperature range studied, and the $\rho(T)$ anomaly is suppressed by fields of 6 T. Magnetoresistance of $Eu_3Pt_7B_2$, on the other hand, is positive at low temperatures as well as in the high-temperature paramagnetic range and negative only in a narrow region around the transition temperature. Despite the ferromagnetic ground state of $Eu_3Pt_7B_2$ leading, in general, to a negative magnetoresistance, the classical magnetoresistance can overcompensate the one originated by magnetic interactions, resulting in an increase of $\rho(T)$ with increasing magnetic fields, at least for certain temperature ranges. The dominance of the classical magnetoresistance in $Eu_3Pt_7B_2$ as compared to $EuPt_4B$ might follow from the fact that the overall resistivity, specifically the residual resistivity, is much lower here than in the case of $EuPt_4B$.

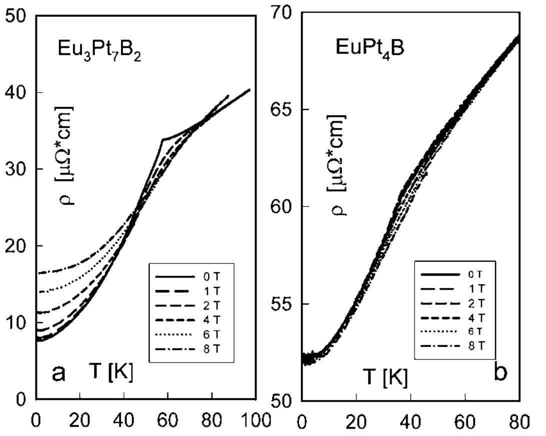

Figure 13. Temperature-dependent electrical resistivity of $Eu_3Pt_7B_2$ (a) and $EuPt_4B$ (b) as a function of magnetic field.

To quantitatively evaluate $\rho(T)$ of $Eu_3Pt_7B_2$, experimental data were first split into two parts, i.e., a low-temperature region (below the magnetic phase transition) and a high-temperature paramagnetic part. In the paramagnetic regime the behavior of the resistivity of $Eu_3Pt_7B_2$ can be described by

$$\rho = \rho_0^* + \rho_{BG}$$

where $\rho_{BG} = C(T^5/\theta_D{}^5)\int_0^{(\theta_D/T)}(x^5/((e^x-1)(1-e^{-x})))$ is the Bloch−Grüneisen term corresponding to the resistivity originated from scattering of conduction electrons on phonons and $\rho^* = \rho_0 + \rho_{mag}$, with ρ_{mag} describing the interaction of conduction electrons with localized magnetic moments. In the absence of crystalline electric field effects, ρ_{mag} is temperature independent in the paramagnetic temperature range. ρ_0 is the residual resistivity. A Debye temperature θ_D = 312 K and ρ^* = 32 $\mu\Omega$·cm were obtained from a least-squares fit in a temperature region over 80 K (dashed line, Figure 12). In the low-temperature region, the resistivity of a ferromagnetic material with spin wave dispersion $\omega \approx k^2$ is expected to behave like $\sim T^2$. Moreover, as a consequence of the enlarged gamma value, derived from the specific heat measurements, the electron−electron scattering should also be taken into account and in turn be proportional to T^2 at low temperatures as well, making it impossible to distinguish between both phenomena. As a result of the fit using $\rho = \rho_0 + AT^2$, ρ_0 = 7.64 $\mu\Omega$·cm was obtained.

The low-temperature part of the resistivity of $EuPt_4B$ is in good agreement with the temperature dependence of a ferromagnetic material. Experimental data are well accounted for by[64] $\rho = \rho_0 + BT\Delta(1 + (2T/\Delta))e^{-\Delta/T}$ with Δ = 12.8 K as the width of the gap in ferromagnetic spin wave spectrum. The high-temperature part, on the other hand, displays some characteristic curvature observed in systems strongly influenced by the crystalline electric field, supporting the mixed-valence hypothesis.

■ SUMMARY

Three new ternary phases have been observed for the first time in the Eu−Pt−B system from arc-melted alloys annealed at 1020 K. Crystal structures have been studied by X-ray single-crystal diffraction and validated by Rietveld refinements of X-ray powder diffraction data. The results beautifully illustrate the structural diversity and versatility of a $CaCu_5$-type derivative family of structures, revealing three different structural series.

$EuPt_4B$ forms a $CeCo_4B$ type and is composed of $CaCu_5$- and $CeCo_3B_2$-type fragments stacked along the *c* axis; $Eu_3Pt_7B_2$ is built of $CeCo_3B_2$- and $MgCu_2$-type slabs and exhibit an ordered variant of $PuNi_3$, namely, $Ca_3Al_7Cu_2$ type with Al and Cu atom sites occupied by Pt and B atoms, respectively. In both compounds the nearest coordination for boron atom is trigonal prism $[BPt_6]$.

Unique stacking of $CaCu_5$-, $CeCo_3B_2$-, and $ThCr_2Si_2$-type slabs has been uncovered in the $Eu_5Pt_{18}B_{6-x}$ structure; the atom arrangement in the $ThCr_2Si_2$-type block is rare for the distribution of Pt and B atoms on Si and Cr atom sites, respectively ($BaAl_4$-type derivative structures), thus changing the coordination of the transition metal as compared to other representatives of a large family of $ThCr_2Si_2$-type compounds and exhibiting chains of edge-connected platinum tetrahedra $[BPt_4]$ running along the *a*-axis direction. With respect to Eu−Eu linkage, the europium atoms are interconnected infinitely along the *c* axis in both $EuPt_4B$ and $Eu_3Pt_7B_2$ structures. The $Eu_5Pt_{18}B_{6-x}$ structure exhibits the repeating blocks of 5 fused polyhedra of Eu linked in a sequence ...−$ThCr_2Si_2$−$CeCo_3B_2$−$CaCu_5$−$CeCo_3B_2$−$ThCr_2Si_2$−...; the units are shifted for a 1/2*a* along the *b*-axis direction with respect to each other, forming blocks which are interlinked via $ThCr_2Si_2$-type fragment along the *c* axis. Positioning of the B atom on the Cr Wyckoff site in the $ThCr_2Si_2$-type slab and consequently its nearest tetrahedral coordination plays a decisive role in formation of $Eu_5Pt_{18}B_{6-x}$ structure, serving as a linking entity (Figure 14) for the repeating structural units of fused Eu polyhedra.

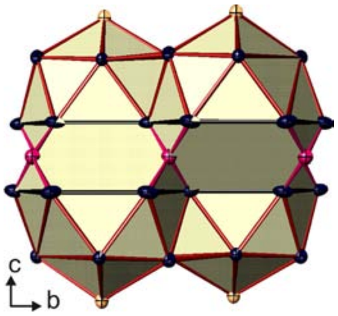

Figure 14. Eu1 polyhedra fused by B-atoms in $Eu_5Pt_{18}B_{6-x}$.

Although $EuPt_4B$ exhibits a feromagnetic ordering at relatively high temperature of 36 K, a mixed-valence state for Eu is observed. In a static case of valence distribution one would expect 50% Eu^{3+} and 50% Eu^{2+} as a consequence of obvious difference between the coordination polyhedra for two Eu atoms unlike our case, where magnetic and specific heat measurements purpose more complex valence behavior. Time-dependent studies are needed to distinguish between a static and a more complex dynamic case of mixed-valence state.

In $Eu_3Pt_7B_2$, the Eu atoms are in the 2+ state and the compound orders feromagnetically at around 57 K. The electron part of specific heat was found to be 206 mJ/mol·K^2, pointing to the existence of strong electron correlations.

■ ASSOCIATED CONTENT

Ⓢ Supporting Information

Single-crystal refinement data for three compounds in CIF format; figures of Rietveld refinements of the X-ray powder diffraction patterns of $EuPt_4B$, $Eu_3Pt_7B_2$, and $Eu_5Pt_{18}B_{6-x}$ ($x = 1$). This material is available free of charge via the Internet at http://pubs.acs.org.

■ AUTHOR INFORMATION

Corresponding Author

*E-mail: ernst.bauer@ifp.tuwien.ac.at (E.B.); peter.franz.rogl@univie.ac.at (P.R.).

Notes

The authors declare no competing financial interest.

■ ACKNOWLEDGMENTS

Research was supported by the Austrian National Science Foundation FWF M1067-N20. L.S. is grateful to the ÖAD for an Ernst Mach fellowship at the Vienna University of Technology.

■ REFERENCES

(1) Rogl, P. Existence and Crystal Chemistry of Borides. In *Inorganic Reactions and Methods*; Zuckerman, J. J., Ed.; VCH Publishers: New York, 1991; Vol. *13*, Chapter 6, pp 85−167.

(2) Parthé, E.; Chabot, B. Crystal Structures and Crystal Chemistry of Ternary Rare Earth-Transition Metal Borides, Silicides and Homologues. In *Handbook on the Physics and Chemistry of Rare Earths*; Gschneidner, K., Jr., Eyring, L., Eds.; Elsevier: Amsterdam, 1984; Vol. *6*, Chapter 48, pp 113−334.

(3) Parthé, E.; Lemaire, R. *Acta Crystallogr., Sect. B* **1975**, *31*, 1879.

(4) Liu, Y.; Pan, H.; Gao, M.; Wang, Q. *J. Mater. Chem.* **2011**, *21*, 4743−4755.

(5) Li, Y.; Shen, J.; Chen, Y. *Solid State Sci.* **2010**, *12*, 33−38.

(6) Hsieh, C. C.; Chang, H. W.; Zhao, X. G.; Sun, A. C.; Chang, W. C. *J. Appl. Phys.* **2011**, *109*, 07A730.

(7) Coey, J. M. D.; Sun, H.; Hurley, D. P. Magnetic materials and processes for their production. U.S. Patent 5478411, 1995.

(8) Kuz'ma, Y. B.; Krypyakevych, P. I.; Bilonizko, N. S. *Dopov. Akad. Nauk Ukr. RSR* **1969**, 939.

(9) Kuz'ma, Y. B. *Crystal Chemistry of Borides*; Vyshcha Shkola: Lvov, 1983.

(10) Jung, W.; Weltzer, M. *Z. Kristallogr.* **1991**, *196*, 169.

(11) Cordier, G.; Czech, E.; Ochmann, H.; Schäfer, H. *J. Less-Common Met.* **1984**, *99*, 173−185.

(12) Salamakha, P.; Sologub, O.; Gonçalves, A. P.; Almeida, M. *J. Alloys Compd.* **2003**, *360*, 131−136.

(13) Jung, W. *J. Less-Common Met.* **1984**, *97*, 253−263.

(14) Sologub, O. L.; Salamakha, L. P.; Noel, H.; Roisnel, T.; Gonsalves, A. *J. Solid State Chem.* **2008**, *180*, 2740−2746.

(15) Higashi, I.; Shishido, T.; Takei, H.; Kobayashi, T. *J. Less-Common Met.* **1988**, *139*, 211−220.

(16) Salamakha, P. S.; Sologub, O. L.; Rizzoli, C.; Hester, J. R.; Stepien-Damm, J.; Gonçalves, A. P.; Lopes, E. B.; Almeida, M. *Intermetallics* **2004**, *12* (12), 1325.

(17) Süllow, S.; Ludoph, B.; Nieuwenhuys, G. J.; Menovsky, A. A.; Mydosh, J. A. *Physica B: Condens. Matter* **1996**, *223−224*, 347−350.

(18) Hermes, W.; Harmening, T.; Pöttgen, R. *Chem. Mater.* **2009**, *21*, 3325−3331 and references therein.

(19) Nonius Kappa CCD, *Program Package COLLECT, DENZO, SCALEPACK, SORTAV*; Nonius: Delft, The Netherlands, 1998.

(20) McArdle, P. *J. Appl. Crystallogr.* **1996**, *29*, 306.

(21) Farrugia, L. J. *J. Appl. Crystallogr.* **1999**, *32*, 837.

(22) Sheldrick, G. M. *SHELXS-97, Program for the Solution of Crystal Structures*; University of Göttingen, Germany, 1997.

(23) Sheldrick, G. M. *SHELXL-97, Program for Crystal Structure Refinement*; University of Göttingen: Göttingen, Germany, 1997.

(24) Speck, A. L. *PLATON. A Multipurpose Crystallographic Tool*; University of Utrecht: The Netherlands, 2003.

(25) Parthé, E.; Gelato, L.; Chabot, B.; Penzo, M.; Censual, K.; Gladyshevskii, R. *TYPIX−Standardized Data and Crystal Chemical Characterization of Inorganic Structure Types*; Springer: Berlin, 1994.

(26) Rodriguez-Carvajal, J. *Physica B* **1993**, *192*, 55.

(27) Bauer, E.; Berger, St.; Paul, Ch.; Della Mea, M.; Hilscher, G.; Michor, H.; Reissner, M.; Steiner, W.; Grytsiv, A.; Rogl, P.; Scheidt, E.-W. *Phys. Rev. B* **2002**, *66*, 214421.

(28) Klünter, W.; Jung, W. *J. Solid State Chem.* **2006**, *179*, 2880–2888.

(29) Filinchuk, Ya.E.; Yvon, K. *Inorg. Chem.* **2005**, *44*, 4398–4406.

(30) Iandelli, A.; Palenzona, A. J. *Less-Common Met.* **1981**, *80*, 71–82.

(31) Nowotny, H. *Z. Metallknd.* **1942**, *34*, 247–253.

(32) Cromer, D. T.; Olsen, C. E. *Acta Crystallogr.* **1959**, *12*, 689.

(33) Villars P. *Pearson's Handbook: Desk Edition Crystallographic Data for Intermetallic Phases*; ASM International, The Materials Information Society: Materials Park, OH, 1998.

(34) Zheng, C. *J. Am. Chem. Soc.* **1993**, *115*, 1047–1051.

(35) Li, B.; Corbett, J. D. *Inorg. Chem.* **2007**, *46* (21), 8812–8818.

(36) Parthe, E.; Chabot, B.; Braun, H. F.; Engel, N. *Acta Crystallogr., Sect. B* **1983**, *39*, 588.

(37) Pearson, W. B. *J. Solid State Chem.* **1985**, *56*, 278.

(38) Häussermann, U.; Amerioun, S.; Eriksson, L.; Lee, C.-S.; Miller, G. J. *J. Am. Chem. Soc.* **2002**, *124*, 4371–4383.

(39) Just, G.; Paufler, P. *J. Alloys Compd.* **1996**, *232*, 1–25.

(40) Tkachuk, A. V.; Mar, A. *J. Solid State Chem.* **2007**, *180* (8), 2298–2304.

(41) Szytula, A.; Leciejewicz, J. *Handbook of Crystal Structures and Magnetic Properties of Rare Earth Intermetallics*; CRC Press: Boca Raton, FL, 1994.

(42) Rotter, M.; Tegel, M.; Johrendt, D. *Phys. Rev. Lett.* **2008**, *101*, 107006–4.

(43) Ishida, K.; Nakai, Y.; Hosono, H. *J. Phys. Soc. Jpn.* **2009**, *78* (6), 062001–20.

(44) Rotter, M.; Tegel, M.; Johrendt, D.; Schellenberg, I.; Hermes, W.; Pöttgen, R. *Phys. Rev. B* **2008**, *78*, 020503.

(45) Rogl, P. *Monatsh. Chem.* **1973**, *104*, 1623–1631.

(46) Rupp, B.; Rogl, P.; Hulliger, F. *J. Less-Common Met.* **1987**, *135*, 113–125.

(47) Niihara, K.; Shishido, T.; Yajima, S. *Bull. Chem. Soc. Jpn.* **1973**, *46*, 1137–1140.

(48) Stepanchikova, G. F.; Kuz'ma, Y. B.; Chernyak, B. I. *Dopov. Akad. Nauk Ukr. RSR, Ser. A* **1974**, *40*, 950.

(49) Jung, W. *Z. Naturforsch. B* **1979**, *34*, 1221–1228.

(50) Mizoguchi, H.; Kuroda, T.; Kamiya, T.; Hosono, H. *Phys. Rev. Lett.* **2011**, *106*, 237001–4.

(51) Petry, K.; Jung, W. *J. Alloys Compd.* **1992**, *183*, 363–376.

(52) Zheng, C.; Hoffmann, R. *Z. Naturforsch.B* **1986**, *41*, 292.

(53) Burdett, J. K.; Miller, G. J. *Chem. Mater.* **1990**, *2*, 12–26.

(54) Jung, W. *J. Less-Common Met.* **1990**, *161*, 375–384.

(55) Felner, I. *J. Phys. Chem. Solids* **1983**, *44*, 43–48.

(56) Jung, W. *J. Less-Common Met.* **1991**, *171*, 119–125.

(57) Luecken, H. *Magnetochemie*; Teubner Studienbücher Chemie: Stuttgart, Leipzig, 1999.

(58) Spaldin, N. A. *Magnetic materials: fundamentals and device applications*; Cambridge University Press: New York, 2003.

(59) Hilscher, G. *J. Magn. Magn. Mater.* **1982**, *25*, 229 and references therein.

(60) Grössinger, R.; Hilscher, G.; Schmitzer, C.; Wohlfarth, E. P. *IEEE Trans. Magn.* **1979**, *15*, 1302.

(61) Baranov, N. V.; Yermakov, A. A.; Markin, P. E.; Possokhov, U. M.; Michor, H.; Weingartner, B.; Hilscher, G.; Kotur, B. *J. Alloys Compd.* **2001**, *329*, 22–30.

(62) Baranov, N. V.; Inoue, K.; Michor, H.; Hilscher, G.; Yermakov, A. A. *J. Phys.: Condens. Matter* **2003**, *15*, 531–538.

(63) Baranov, N. V.; Michor, H.; Hilscher, G.; Proshkin, A.; Podlesnyak, A. *J. Phys.: Condens. Matter* **2008**, *20*, 325233.

(64) Jobiliong, E.; Brooks, J. S.; Choi, E. S.; Lee, H.; Fisk, Z. *Phys. Rev. B* **2005**, *72*, 104428.